The Astrophysical Journal, 864:149 (18pp), 2018 September 10 https://doi.org/10.3847/1538-4357/aad6e9

VEGAS: A VST Early-type Galaxy Survey. III. Mapping the Galaxy Structure, Interactions, and Intragroup Light in the NGC 5018 Group

Marilena Spavone[1], Enrichetta Iodice[1], Massimo Capaccioli[2], Daniela Bettoni[3], Roberto Rampazzo[3], Noah Brosch[4], Michele Cantiello[5], Nicola R. Napolitano[1], Luca Limatola[1], Aniello Grado[1], and Pietro Schipani[1]
[1] INAF–Astronomical Observatory of Capodimonte, Salita Moiariello 16, I-80131, Naples, Italy; marilena.spavone@oacn.inaf.it
[2] University of Naples Federico II, C.U. Monte Sant'Angelo, via Cinthia, I-80126, Naples, Italy
[3] INAF-Astronomical Observatory of Padova, Vicolo dell'Osservatorio 5, I-35122, Padova, Italy
[4] The Wise Observatory and School of Physics and Astronomy, Tel Aviv University, Israel
[5] INAF–Astronomical Observatory of Teramo, Via Maggini, I-64100, Teramo, Italy
Received 2018 May 9; revised 2018 July 27; accepted 2018 July 27; published 2018 September 11

Abstract

Most of the galaxies in the universe today are in groups, which are key to understanding their evolution. In this work we present a new deep mosaic of 1.2 × 1.0 square degrees of the group of galaxies centered on NGC 5018, acquired at the ESO VLT Survey Telescope. We use *u*, *g*, *r* images to analyze the structure of the group members and to estimate the intragroup light. Taking advantage of deep and multiband photometry and of the large field of view of the VST telescope, we studied the structure of the galaxy members and the faint features leading into the intragroup space, and we give an estimate of the intragroup diffuse light in the NGC 5018 group of galaxies. We found that ∼41% of the total *g*-band luminosity of the group is in the form of intragroup light (IGL). The IGL has a $(g - r)$ color consistent with those of other galaxies in the group, indicating that the stripping leading to the formation of IGL is ongoing. From the study of this group we can infer that there are at least two different interactions involving the group members: one between NGC 5018 and NGC 5022, which generates the tails and ring-like structures detected in the light, and another between NGC 5022 and MCG-03-34-013, which has produced the H I tail. A minor merging event also happened in the formation history of NGC 5018 that perturbed the inner structure of this galaxy.

Key words: galaxies: elliptical and lenticular, cD – galaxies: formation – galaxies: fundamental parameters – galaxies: halos – surveys

1. Introduction

The hierarchical, merger-dominated picture of galaxy formation predicts that the observed galaxies and their dark halos (DHs) were formed through repeated merging processes of small systems (De Lucia et al. 2006). Under this paradigm, clusters of galaxies are the most recent objects to form, and their central galaxies continue to undergo active mass assembly and accretion of smaller groups.

Throughout this cluster assembly, individual galaxies interact with one other. During these interactions, matter can be stripped from galaxies and form tidal tails, shells, bridges, thus liberating stars from their host galaxies, which contributes to the formation of a very faint component of diffuse intracluster light (ICL) (Mihos 2015).

According to this picture, any star that becomes unbound from its host galaxy contributes to the growth of ICL, which can then be considered as the fossil record of all the past interactions. If so, the main properties of the ICL, such as color, metallicity, and spatial distribution, are closely linked to the properties of galaxies in which intracluster stars originate, and they can help to disentangle their formation history.

In the group environment, interactions between galaxies are slow, leading to a strong tidal stripping of material and to the formation of tidal debris, which is mixed into the ICL when the groups fall into the cluster. In situ star formation can also occur in the intracluster medium, due to the presence of gas stripped from infalling galaxies that contributes to feeding the ICL. Following this evolutionary picture, the diffuse intragroup light (IGL) can be considered as a precursor to the ICL in massive clusters of galaxies.

Since groups contain most of the galaxies in the universe (∼60%) today, the group environment is of particular interest for the study of the intragroup starlight. IGL is in fact quite evident in strongly interacting groups, given that the strong interactions are able to expel diffuse material out to large distances (Da Rocha & Mendes de Oliveira 2005; Watkins et al. 2015).

In the last decade, a big effort was made to determine the amount and spatial distribution of IGL in both normal and compact groups, both observationally and theoretically.

Theoretical studies give conflicting predictions on the fraction of the IGL component and of its variation with the group mass. Numerical simulations by Napolitano et al. (2003), Lin & Mohr (2004), Murante et al. (2004, 2007), Purcell et al. (2007), Watson et al. (2012), and Tollet et al. (2017) predict a strong evolution of the ICL and IGL fraction with the cluster and group mass, while Krick & Bernstein (2007) found an anticorrelation between the ICL/IGL fraction and the cluster/group mass. Contini et al. (2014) found that the fractions of ICL and IGL predicted by their models range between 10% and 40% and that they do not vary as a function of the mass. Models by Sommer-Larsen (2006) and Rudick et al. (2006) show that from 12% to 45% of the light in groups is in the form of IGL, and that the fractions of IGL/ICL can be used as a "dynamical clock," since they increase with the degree of dynamical evolution of the group/cluster (i.e., more evolved groups/clusters have larger fractions of diffuse light).

On the observational side, the diffuse IGL/ICL component has been mapped using several observational techniques, such as deep imaging (Feldmeier et al. 2002; Mihos et al. 2005;

Zibetti et al. 2005), the detection of red giant branch stars associated with the diffuse stellar component (Williams et al. 2007), and intracluster planetary nebulae (Arnaboldi et al. 2002, 2004; Aguerri et al. 2005, 2006; Gerhard et al. 2005, 2007; Castro-Rodriguéz et al. 2009; Longobardi et al. 2013, 2015).

The fraction of IGL has been estimated in some compact groups of galaxies. Da Rocha & Mendes de Oliveira (2005) and Da Rocha et al. (2008) found smooth envelopes of diffuse light around the galaxy groups studied, and estimated IGL fractions of 11%–46%, with colors compatible with those of galaxies in the groups. They also suggest an evolutionary sequence for the analyzed groups, i.e., groups with the highest IGL fraction are in a more advanced phase of their dynamical evolution than groups with smaller fractions of IGL. Also White et al. (2003) found a consistent amount of IGL (38%–48%) in the compact group HCG 90, with a color distribution consistent with an old stellar population, while Aguerri et al. (2006) found an IGL fraction of 4.7% for the group HCG 44. In contrast, Watkins et al. (2017) found no diffuse light in the group M96. DeMaio et al. (2018) studied the properties of 23 galaxy groups and found that the bright cluster galaxies (BCGs) together with the ICL constitute a higher fraction of the total mass in groups than in clusters, and that the group environments are more efficient ICL producers. McGee & Balogh (2010) studied spectroscopically confirmed intragroup Type Ia supernovae and inferred that 47% of the stellar mass in the analyzed galaxy groups was in the form of IGL.

The study of intracluster planetary nebulae in two fields of the Virgo cluster, by Arnaboldi et al. (2004), revealed that the diffuse light contributes from 17% to 43% of the total (i.e., galaxies + diffuse light) luminosity density in the imaged fields. Castro-Rodríguez et al. (2003), by carrying out a wide-field survey for emission line objects associated with the intragroup H I cloud in the Leo group, have been able to set an upper limit for the ratio of diffuse intragroup light to galaxy light that is ∼1.6%. Castro-Rodriguéz et al. (2009) used planetary nebulae detected in several regions of the Virgo cluster to derive a fraction of ICL of ∼7% of the total light in Virgo cluster galaxies.

Recently, wide-field and deep photometric studies have revealed the presence of diffuse IGL even in the less dense environment of loose groups (Ibata et al. 2014; Okamoto et al. 2015), where slow encounters are particularly effective at liberating stars from galaxies in the intragroup medium. Loose groups of galaxies are intermediate in scale between galaxies and rich clusters, and due to their irregular nature their definition is ambiguous. Their environment is also intermediate between that of isolated galaxies and that of the cores of rich clusters, and therefore the study of IGL in these environments is of particular interest, given that it can give clues to the evolution of galaxies and galaxy clusters.

Despite these many programs aimed at the study of the IGL/ICL in a variety of different systems in different dynamical states, there are still observational and interpretational difficulties to face, which make the investigation of the IGL and ICL not a trivial task. Over the past decade many observational studies of these diffuse components have been carried out, but despite this the amount of ICL is hard to estimate. First, the ICL and IGL components are diffuse and have very faint levels of surface brightness, which demands the use of accurate techniques to correctly estimate all sources of contamination. Second, the IGL/ICL is strictly connected to the BCGs, and using photometry it is not always possible to distinguish the diffuse (unbound) component from the extended (likely bound) stellar halos of the BCGs.

In the recent years, a great boost to these researches has been given by deep photometric surveys aimed at studying galaxy structures out to the regions of the stellar halos, where the galaxy light merges into the intracluster component (Ferrarese et al. 2012; Duc et al. 2015; Muñoz et al. 2015; Merritt et al. 2016). The VST Early-type Galaxy Survey (VEGAS) (see http://www.na.astro.it/vegas/VEGAS/Welcome.html) is just a part of this campaign and it is producing competitive results. From the surface photometry for the cD galaxy NGC 4472, a tail of intracluster light was detected in the region $5\,R_e \leqslant R \leqslant 10\,R_e$, in the range of surface brightness of 26.5–27.6 mag arcsec^{-2} in the g band (Capaccioli et al. 2015). New results on six massive early-type galaxies (including NGC 4472) in VEGAS confirm the feasibility of such a survey to reach the faint surface brightness levels of 27–30 mag arcsec^{-2} in the g band, out to $\sim 10 R_e$ (Spavone et al. 2017). Therefore, taking advantage of the deep photometry, the growth history of the stellar halo can be addressed by comparing the surface brightness profile and the stellar mass fraction with the prediction of cosmological galaxy formation.

As part of VEGAS, the Fornax Deep Survey (FDS) at VST (VLT Survey Telescope) covers the Fornax cluster out to the virial radius (∼0.7 Mpc), with an area of about 26 square degrees around the central galaxy NGC 1399, and including the SW subgroup centered on Fornax A. First results have provided the largest mosaics to date, which cover an area of 3 × 6 square degrees around the central galaxy NGC 1399 (see the ESO photo release at https://www.eso.org/public/news/eso1612/) and an area of ∼4 × 2 square degrees around the central galaxy NGC 1316 of the SW group of the Fornax cluster (Iodice et al. 2016, 2017b). The deep photometry, the high spatial resolution of OmegaCam, and the large area covered allow one: (i) to map the surface brightness around NGC 1399 and NGC 1316 out to an unprecedented distance of ∼200 kpc down to $\mu_g \simeq 29$–31 mag arcsec^{-2} (Iodice et al. 2016, 2017b); (ii) to trace the spatial distribution of candidate globular clusters (GCs) inside ∼0.5 deg^2 of the cluster core (D'Abrusco et al. 2016; Cantiello et al. 2018); (iii) to detect new and faint ($\mu_g \simeq 28$–30 mag arcsec^{-2}) features in the intracluster region between NGC 1399 and NGC 1387 (Iodice et al. 2016) and in the outskirts of NGC 1316 (Iodice et al. 2017b); and (iv) to detect an unknown region of ICL in the core of the cluster, on the west side of NGC 1399 (Iodice et al. 2017a).

Thanks to the coverage of different morphological types, masses, and environments in VEGAS, we have started a study dedicated to the synoptic analysis of GC systems in different host galaxies. As an example, preliminary results from GCs in NGC 3115 and NGC 1399 support the scenario where the red/metal-rich GC component is bound to the galaxy, while the blue/metal-poor GCs are gravitationally associated with a cluster-wide component, if present (Cantiello et al. 2018).

In this work we present a new deep mosaic of 1.2 × 1.0 square degrees of the group of galaxies centered on NGC 5018, acquired at the ESO VST. We use *u, g, r* images to analyze the structure of the group members and to estimate the intragroup light. This work represents a pilot study in the framework of the

VEGAS survey to study the IGL components in the less dense environments of the groups.

We adopt a distance for NGC 5018 of $D = 40.9$ Mpc (Tully 1988), therefore the image scale is 198.3 pc arcsec^{-1}.

The plan of the paper is the following. In Section 2 we present the properties of NGC 5018 as found in the literature, while in Section 3 we describe the data used in this work, as well as the adopted observing strategy and the data reduction. In Sections 4–6 the photometric optical, infrared, and ultraviolet analyses are described. In Section 7 we present the 1D fitting procedure adopted and the derived accreted mass fractions of galaxies in the group. In Section 8 we draw our conclusions.

2. NGC 5018 in the Literature

NGC 5018 is the brightest member of a small group of five galaxies (Gourgoulhon et al. 1992), which also consists of the edge-on spiral NGC 5022, the S0 galaxy MCG-03-34-013, and the two face-on dwarf, gas-rich ($\sim 10^8\,M_\odot$) spirals labeled S2 and S3 by Kim et al. (1988) (see Figure 1). Kim et al. (1988), adopting a distance $D \sim 22.5\,h^{-1}$ Mpc, also estimate that the group has a size of $\sim$200 kpc and a total mass of $\sim 4 \times 10^{12}\,M_\odot$. Despite its classification as a "normal" elliptical, NGC 5018 shows several signs of a past interaction event, such as a very complex system of dust lanes, shells, a tail on the NW side, and a prominent bridge of gas toward the companion galaxy NGC 5022. The galaxy is also present in the list of shell galaxies revealed by Malin & Carter (1983).

The H I mass associated to NGC 5018, estimated by Kim et al. (1988), is $\sim 4 \times 10^8\,M_\odot$, while the same authors found that the H I in NGC 5022 is distributed in a rotating disk, with a mass of $\sim 2 \times 10^9\,M_\odot$.

Follow-up H I observations made by Guhathakurta et al. (1990) showed that the H I bridge actually connects NGC 5022 with MCG-03-34-013, while it bifurcates at the position and radial velocity of NGC 5018. They also estimate that the interaction that led to the formation of the northern plume was recent ($\sim 6 \times 10^8$ Gyr). Guhathakurta et al. (1990) assert that their H I and optical data provide direct observational evidence for the formation of a shell system, through the merger of an elliptical galaxy with a cold disk system.

Many authors have also found the presence of a young ($\sim$3 Gyr) and dominant stellar population in the central regions of NGC 5018 (Bertola et al. 1993; Carollo & Danziger 1994; Leonardi & Worthey 2000; Buson et al. 2004; Rampazzo et al. 2007), with a near solar metallicity. The peculiarities found in NGC 5018, such as a lower metallicity than giant ellipticals, the presence of an Mg_2 index much weaker than those of ellipticals of similar absolute magnitude, the low UV flux level, the presence of bluer shells, a complex system of dust lanes, and a bridge of H I connecting NGC 5018 with NGC 5022, pose serious problems to the classical picture of the formation of elliptical galaxies.

Bertola et al. (1993) proposed two possible scenarios for the formation of this peculiar galaxy. The first scenario is the merging of many separate smaller galaxies, having low metallicities, while the other possibility is its formation ab initio with low metallicity and a subsequent, recent merger with a small disk galaxy, which is able to reproduce the morphological peculiarities of NGC 5018. Bertola et al. (1993) discounted dust obscuration as the cause of the low UV flux level because the best photometry available at that time showed that the dust lane does not cover the regions of their UV spectra. Later, Carollo & Danziger (1994) showed the presence of dust up to the very central regions, demonstrating that the reddening effect was not negligible.

Leonardi & Worthey (2000) derived a robust reddening-insensitive estimate of the age of the young stellar population in the central regions of NGC 5018. The estimated age of 2.8 Gyr for this population, which dominates the visible part of the spectrum, also explains the small UV flux with no need to invoke a large amount of dust obscuration.

NGC 5018 has been examined by Rampazzo et al. (2013) using the *Spitzer* infrared spectrograph (IRS) in the range 4–38 μm (see in particular their Figure 5). The galaxy nucleus shows features of polycyclic aromatic hydrocarbons (PAHs) with interband ratios typical of late-type galaxies. These PAH features are present only in a fraction of 9^{+4}_{-3}% of early-type galaxies in the Revised Shapley–Ames Catalog examined by Rampazzo et al. (2013). This suggests that NGC 5018 has a still actively star-forming nuclear region, since IRS (SL+LL) spectra integrate in a projected region of 0.7×3.3 kpc^2.

Hilker & Kissler-Patig (1996) studied the properties of the GCs of NGC 5018. They detected a poor GC system, which can be divided into two populations: a small population of blue GCs, with ages between several hundred Myr and 6 Gyr, and one or two populations of older GCs. The first population was probably formed during the last interaction, while the second one is associated with the original galaxy. Another peculiarity of this galaxy is the distribution of GCs; Hilker & Kissler-Patig (1996) found that blue GCs are missing in a stripe extending from southeast to north of the galaxy and that red GCs are instead overabundant in this same stripe. The inhomogeneous distribution of the H I found by Guhathakurta et al. (1990) could be responsible for the inhomogeneous distribution of GCs, but this cannot explain the overabundance of red objects in the stripe. The small number of young GCs found in NGC 5018 ($\sim$10%) is evidence against a significant increase in GCs by a merger event for this galaxy.

NGC 5018 was also observed in X-rays with the *Chandra X-Ray Observatory*'s Advanced CCD Imaging Spectrometer by Ghosh et al. (2005). These authors found six non-nuclear X-ray point sources in NGC 5018, as well as diffuse hot gas that may be the remnant of interactions of NGC 5018 with its neighboring galaxies. Their total absorption-corrected luminosity for the diffuse light was $(13.7 \pm 1.5) \times 10^{39}$ erg s^{-1}. Ghosh et al. (2005) also estimated a radiative cooling time for the hot plasma of a few times 10^7 to 10^8 yr, which turns to be shorter than the age of the last interaction (Guhathakurta et al. 1990). They conclude that the gas is still falling in and that it is reheated by ionization, stellar winds, and supernovae caused by recent star formation activity. Moreover, they found that, even if there is little current star formation in NGC 5018, there is a significant reservoir of gas that maintains a low but steady level of star formation, also explaining the diffuse X-ray emission of the galaxy.

Recently, *Chandra* X-ray data have been analyzed by Smith et al. (2018) to study the diffuse X-ray-emitting gas in major mergers. They made a rough classification of the systems in

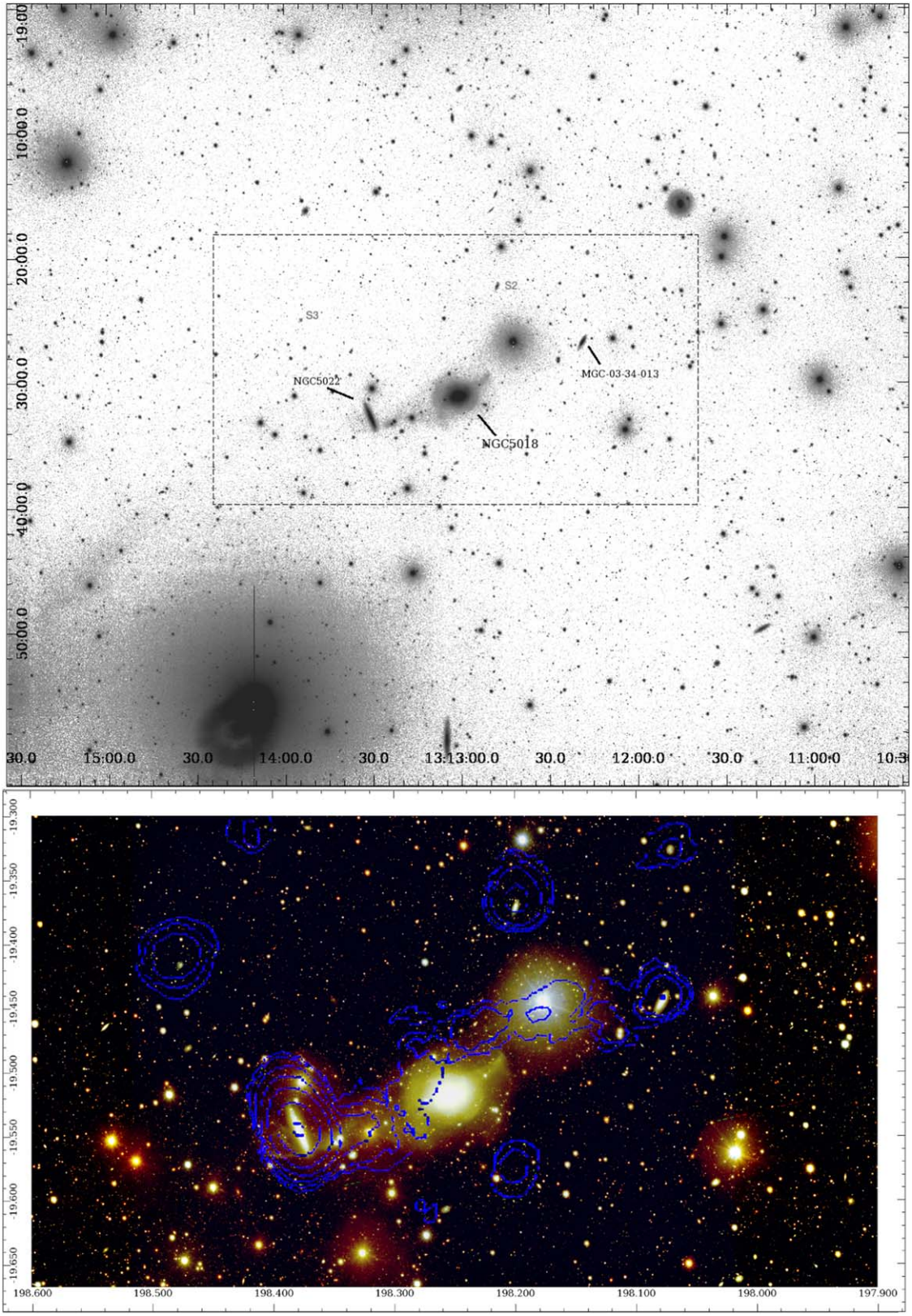

Figure 1. Top: VST *g*-band mosaic of the NGC 5018 group. The image size is $1.^{\circ}2 \times 1.^{\circ}0$. Bottom: color composite image of the central regions of the group ($0.^{\circ}7 \times 0.^{\circ}4$), assembled from *u*-, *g*-, and *r*-band VST images, with the H I map from the Very Large Array (VLA) superimposed (blue contours), adapted from Kim et al. (1988).

their sample into seven merger stages. According to the adopted criteria, they classify NGC 5018 as a very late-stage major merger remnant.

In summary, our present knowledge converges in indicating that in NGC 5018 one or more merging episodes may have characterized its recent history. With the study of the IGL we

aim to add a new tessera in the mosaic considering its evolutionary environment.

3. Observations and Data Reduction

The data presented in this work are part of the VEGAS[6] survey, which is a multiband u, g, r, and i imaging survey, obtained with the ESO VLT Survey Telescope (VST).

With VEGAS we are mapping the light distribution and colors out to 8–10 R_e[7] and down to $\mu \sim 30$ mag arcsec^{-2} in the g band, for a large sample ($\sim$42) of early-type galaxies (ETGs) in different environments, including giant cD galaxies in the core of clusters. The main science goal of VEGAS is to study (i) the galaxy structure and its faint stellar halo, including the diffuse light component, inner substructures as signatures of recent cannibalism events, inner disks, and bars; (ii) the external low-surface-brightness structures of the galaxies (tidal tails, stellar streams, and shells) and their connection with the environment; (iii) for those galaxies in the sample with $D < 40$ Mpc, the GCs and galaxy satellites in the outermost regions of the host galaxy and their photometric properties (e.g., GC colors and mean GC radial color changes). A more detailed description of the survey, the selected targets, and the main scientific aims can be found in Capaccioli et al. (2015). The data reduction, performed by using the VST-Tube pipeline (Grado et al. 2012), and the analysis are described in detail by Capaccioli et al. (2015), Spavone et al. (2017), and Iodice et al. (2016, 2017a).

The most important step of the data processing is the estimation and subtraction of the sky background. For this reason, we adopt a *step dither* observing strategy for galaxies with large angular extent, since it allows a very accurate estimate of the sky background (Iodice et al. 2016, 2017a; Spavone et al. 2017). This strategy consists of a cycle of short exposures centered on the target and on offset fields ($\Delta \sim \pm 1°$). With such a technique the background can be estimated from exposures taken as close as possible, in space and time, to the scientific images. This ensures better accuracy, reducing the uncertainties at very faint surface brightness levels. This observing strategy allowed us to build an average sky background of the night, which was subtracted from each science image. This average sky frame takes into account the small contribution to the sky brightness from the smooth components plus the extragalactic background light. The residual fluctuations in the background are then estimated, and taken into account, by using the methodology described by Pohlen & Trujillo (2006), as explained in Spavone et al. (2017). These fluctuations of the sky background have been taken into account in the error estimates we quote on our surface brightness measurements.

In the case of NGC 5018 we adopted as offset field the one located at the west side of the galaxy (R.A. $13^h08^m47^s.260$, decl. $-19^d20^m46^s.40$), since this field is not very crowded, and mainly because it does not contain very bright galaxies and stars.

The data used in this paper consist of exposures in u, g, and r bands obtained with VST + OmegaCAM, in visitor mode (run IDs: 096.B-0582(B), 097.B-0806(A), and 099.B-0560(A)), during dark time, in photometric conditions, with an average seeing between 0.6 and 1.1 arcsec (see Table 1). In this work we analyze an area of 1.2 square degrees around NGC 5018. This area covers the three main galaxies of the small group—the dominant early-type galaxy NGC 5018, the edge-on spiral NGC 5022, and the S0 galaxy MCG-03-34-013—analyzed in this work, whose main properties are listed in Table 2.

Table 1
VST Exposures Used in This Work

Object	Band	T_{exp} (s)	FWHM[a] (arcsec)
NGC 5018	u	8280	0.77
	g	8280	0.77
	r	8280	0.94

Note.
[a] Median value of the FWHM.

Table 2
Basic Properties of the Galaxies Studied in This Paper

Parameter	Value	References[a]
	NGC 5018	
Morphological type	E3	RC3
R.A. (J2000)	$13^h13^m01^s.0$	NED
Decl. (J2000)	$-19^d31^m05^s$	NED
Helio. radial velocity	2816 km s^{-1}	NED
Distance	40.9 Mpc	Tully (1988)
	NGC 5022	
Morphological type	SBb pec	RC3
R.A. (J2000)	$13^h13^m30^s.8$	NED
Decl. (J2000)	$-19^d32^m48^s$	NED
Helio. radial velocity	3001 km s^{-1}	NED
Distance	40.4 Mpc	NED
	MCG-03-34-013	
Morphological type	S0	RC3
R.A. (J2000)	$13^h12^m18^s.9$	NED
Decl. (J2000)	$-19^d26^m46^s$	NED
Helio. radial velocity	2691 km s^{-1}	NED
Distance	40.7 Mpc	NED

Note.
[a] RC3 is the Third Reference Catalog of Bright Galaxies. NED is the NASA/IPAC Extragalactic Database.

4. Surface Photometry

4.1. Isophotal Analysis

The isophotal analysis of the galaxies in this work is performed on the final mosaic in each band with the IRAF[8] task ELLIPSE.

In the top panel of Figure 2 we show the VST g-band image of NGC 5018, NGC 5022, and MCG-03-34-013, in surface brightness levels. In the bottom-left panel of the same figure we show the ellipticity (ϵ) and position angle (P.A.) profiles in the g band (blue points), r band (red points), and u band (green points) resulting from our isophotal analysis, performed via the ELLIPSE task as described in detail in Spavone et al. (2017). The bottom-right panel shows the g-, r-, and u-band VST

[6] http://www.na.astro.it/vegas/VEGAS/Welcome.html
[7] R_e is the effective radius of a galaxy.
[8] IRAF (Image Reduction and Analysis Facility) is distributed by the National Optical Astronomy Observatories, which is operated by the Associated Universities for Research in Astronomy, Inc. under cooperative agreement with the National Science Foundation.

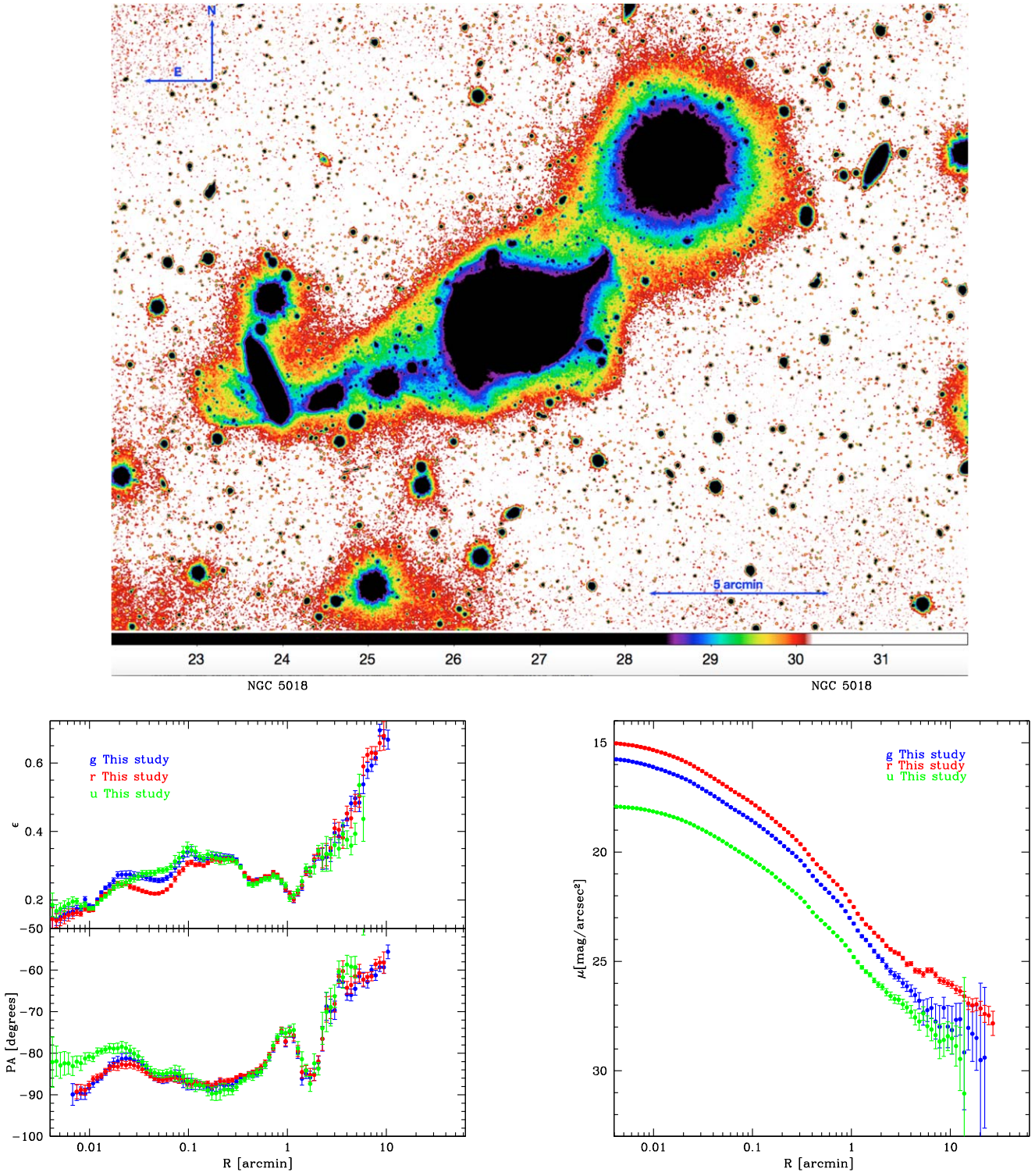

Figure 2. Top: VST g-band sky-subtracted image of the $0.^{\circ}4 \times 0.^{\circ}4$ field around NGC 5018. The color scale represents surface brightness in mag arcsec^{-2}. Bottom left: ellipticity (ϵ) and position angle (P.A.) profiles for NGC 5018, in the g band (blue points), r band (red points), and u band (green points). Bottom right: azimuthally averaged surface brightness profiles in the g (blue), r (red), and u (green) bands.

azimuthally averaged surface brightness profiles of NGC 5018. No correction for blurring due to seeing is applied to the inner regions of the profiles.

The same isophotal analysis has been performed also for NGC 5022 and MCG-03-34-013, and the results are shown in Figures 3 and 4, respectively.

The growth curves obtained by isophote fitting have been extrapolated to derive total magnitudes m_T, effective radii R_e, and corresponding effective magnitudes μ_e in each band (Table 3). All the reported magnitudes are corrected for interstellar extinction by using extinction coefficients derived by Burstein & Heiles (1982).

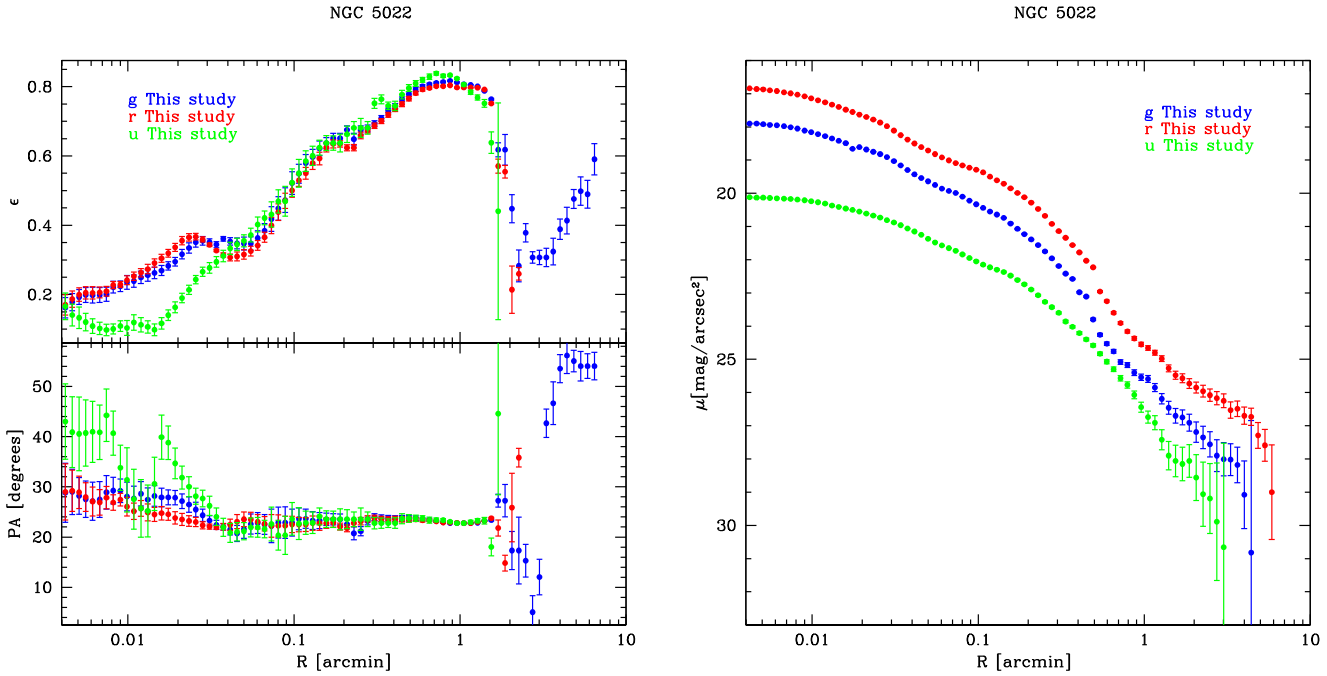

Figure 3. Left: ellipticity (ϵ) and position angle (P.A.) profiles for NGC 5022, in the g band (blue points), r band (red points), and u band (green points). Right: azimuthally averaged surface brightness profiles in the g (blue), r (red), and u (green) bands.

4.2. Two-dimensional Model of the Light Distribution

The IRAF task BMODEL creates a two-dimensional image file containing a noiseless photometric model of a source image ("parent image"). The model is built from the results of isophotal analysis generated by the isophote fitting task, ELLIPSE. We use BMODEL to create a model of NGC 5018, which is able to take into account also variations in ellipticity and P.A. In Figure 5 we show the residual image obtained by subtracting the galaxy model from the VST g-band image.

The complex structure of NGC 5018 stands out very clearly from the residual image. From this map, in fact, we can clearly identify a number of substructures, such as a prominent tail in the NW side of the galaxy, the bridge connecting NGC 5018 with NGC 5022, and the loop on the SE side of NGC 5022, which were also visible in the "parent image," as well as multiple shells, filaments, and fans of stellar light, extending to the central regions of the galaxy.

We used the method described by Tal et al. (2009) to quantify the tidal disturbance of NGC 5018, by dividing the masked VST g-band image of the galaxy and the galaxy model obtained as explained above. The resulting model frame is shown in Figure 6.

This figure shows even more clearly the complex system of dust lanes in the central regions of the galaxy, as well as its multiple shells and fans of diffuse material. NGC 5018, in fact, has been classified by Tal et al. (2009) as a "highly disturbed galaxy," on the basis of its tidal parameter. According to these authors, such a complex system is probably the result of mergers with multi-component objects such as S0 or spiral galaxies.

4.3. Color Distribution

We have derived the azimuthally averaged, extinction-corrected $(g - r)$ and $(u - g)$ color profiles (Figure 7, bottom panel) and the 2D color maps centered on NGC 5018 (top and middle panels). On average, central regions are bluer than the outer ones, but the colors are consistent with those typically found for ETGs (La Barbera et al. 2012). The complex system of dust lanes in the center of the galaxy is evident from both the color maps.

Azimuthally averaged, extinction-corrected, $(g - r)$ and $(u - g)$ color profiles have been derived also for NGC 5022 and MCG-03-34-013, and are shown in the bottom panels of Figure 7.

By using the residual map shown in Figure 5, we derived the integrated $(g - r)$ colors in the substructures standing out from this map. To this aim, after masking all the bright sources, we define on the residual map a set of polygons covering such substructures, and use them to estimate the integrated colors, with the main goal being to compare them with those of the galaxies belonging to the group. In Figure 8 we show the integrated colors of the different polygons, compared with those of the galaxies ($(g - r)_{\rm NGC\ 5018} = 0.67 \pm 0.02$, $(g - r)_{\rm NGC\ 5022} = 0.73 \pm 0.02$, $(g - r)_{\rm MCG-03-34-013} = 0.62 \pm 0.02$), marked as dashed red lines in the plot.

From this comparison, shown in Figure 8, we can see that substructures labelled as 1 ($(g - r) = 0.97$), 5 ($(g - r) = 0.9$), 10 ($(g - r) = 1.08$), and 11 ($(g - r) = 1.1$) have colors consistent with each other, but redder than those of the galaxies in the group. This suggests that all the above features are part of a single structure, which could have an external origin, since its color is not compatible with any of the galaxies in the group. Moreover, we can note that the colors of these substructures are comparable with those of the outskirts of both NGC 5018 and NGC 5022. The implications of this result will be discussed in Section 8.

The colors of all the other identified substructures appear to be similar to that of NGC 5018, suggesting that they could be part of the parent galaxy.

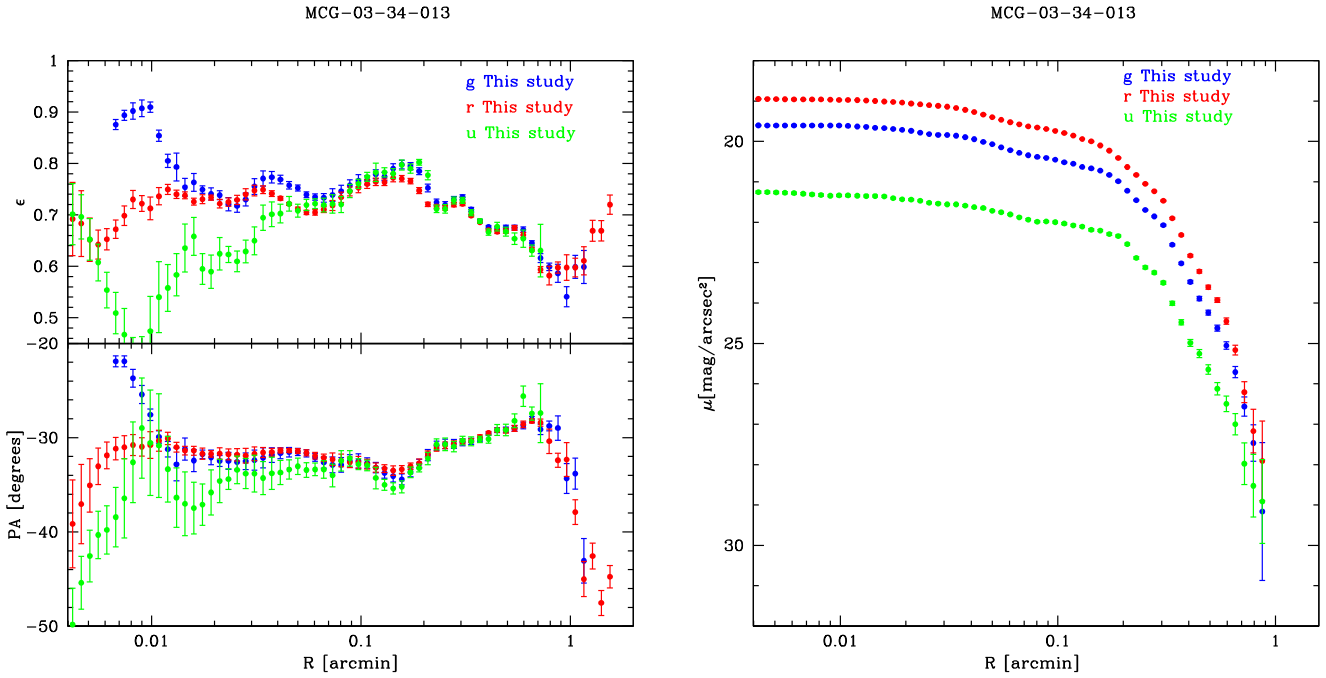

Figure 4. Left: ellipticity (ϵ) and position angle (P.A.) profiles for MCG-03-34-013, in the g band (blue points), r band (red points), and u band (green points). Right: azimuthally averaged surface brightness profiles in the g (blue), r (red), and u (green) bands.

4.4. Integrated Colors of the Intragroup Light

We used the IRAF task POLYMARK to define a region in the residual map centered on NGC 5018 (see Figure 5) covering the bulk of the IGL. Then we use POLYPHOT to derive the integrated magnitudes in the g and r bands, and $(g - r)$ color inside this area. Foreground and background bright sources have been masked and excluded from the estimate of the integrated quantities (see also Iodice et al. 2017a).

The extinction-corrected magnitudes and color derived are $m_g^{\rm IGL} = 11.39 \pm 0.29$ mag, $m_r^{\rm IGL} = 10.61 \pm 0.07$ mag, and $(g - r) = 0.78 \pm 0.35$ mag, and then the total luminosity in the g band is $L_g^{\rm IGL} = 7.06 \times 10^{10}\, L_\odot$. The fraction of IGL with respect to the total luminosity of the group ($L_g = 1.7 \times 10^{11}\, L_\odot$) is about 41%, while that with respect to the dominant galaxy NGC 5018 ($L_g = 1.5 \times 10^{11}\, L_\odot$) is about 47%. The integrated $(g - r)$ color of the IGL component is consistent with those of the galaxies in the group, within the errors.

Given that the IGL is composed of stars stripped from galaxies, its color relative to the galaxies can give indications of the epoch when it was stripped. In particular, if the IGL is redder than the group galaxies, it is likely that stars have been stripped from the galaxies at early times, while if the color of the IGL is similar to that of galaxies, it is likely that this component has formed from the ongoing stripping of stars (Krick et al. 2006).

The ongoing stripping scenario is consistent with our results. Moreover, the color of the IGL component is also roughly consistent, within the errors, with the color of the outskirts of NGC 5018. Simulations by Willman et al. (2004) predict that ∼50% of intragroup stars come from bright galaxies, and as a consequence the color of the intragroup stars should be consistent with the color of the outskirts of bright group galaxies.

5. Infrared Analysis

As shown in the previous sections, the photometric analysis in the optical bands has shown the presence of a prominent and complex system of dust lanes crossing the central regions of NGC 5018. Since the dust optical depth decreases toward longer wavelengths, near-infrared (NIR) photometry can help to reduce the dust absorption, which strongly affects the distribution of starlight in the galaxy. Moreover, adding some infrared bands to the photometric analysis could help to better understand the nature of the bridge connecting NGC 5018 to NGC 5022.

In this work we use images obtained with the *Wide-field Infrared Survey Explorer* (*WISE*, Wright et al. 2010) in the *w1* (3.368 μm) and *w2* (4.618 μm) bands, to perform the infrared photometric analysis for NGC 5018. The results of this analysis are shown in Figure 9, where we plot the profiles of ϵ and P.A. (top panel), the azimuthally averaged surface brightness profiles (middle panel), and the mean $(w1 - w2)$ color profile (bottom panel).

In order to better constrain the nature of the substructures observed in the optical residual map of NGC 5018, we applied the same procedure described in Section 4.3 to the NIR residual map. We used the same polygons obtained above (see Figure 5) to estimate the integrated NIR color of the substructure standing out from the map. We also derived the integrated colors for NGC 5018 ($(w1 - w2) = 0.02$), NGC 5022 ($(w1 - w2) = 0.05$), and MCG-03-34-013 ($(w1 - w2) = -0.01$), in order to compare them with the colors of the different substructures. The results are shown in Figure 10, where we plot the infrared colors of the different substructures compared with those of the three galaxies of the group.

This analysis confirms that also the NIR colors of the substructures number 1 ($(w1 - w2) = 0.1$) and number 5 ($(w1 - w2) = 0.09$), as well as those of the bridge (labelled as 10,

Table 3
Distances and Photometric Parameters for the Sample Galaxies

Object	D (Mpc) (a)	A_u (mag) (b)	A_g (mag) (b)	A_r (mag) (b)	$\mu_{e,u}$ (mag arcsec^{-2}) (c)	$r_{e,u}$ (arcmin)	$m_{T,u}$ (mag) (c)	$M_{T,u}$ (mag) (c)	$\mu_{e,g}$ (mag arcsec^{-2}) (c)	$r_{e,g}$ (arcmin)	$m_{T,g}$ (mag) (c)	$M_{T,g}$ (mag) (c)	$\mu_{e,r}$ (mag arcsec^{-2}) (c)	$r_{e,r}$ (arcmin)	$m_{T,r}$ (mag) (c)	$M_{T,r}$ (mag) (c)
NGC 5018	40.9	0.493	0.362	0.263	24.98	1.40	11.71	−21.35	21.92	0.54	10.93	−22.49	24.68	3.41	9.29	−23.77
NGC 5022	40.4	0.513	0.377	0.274	23.83	0.43	14.09	−18.94	21.67	0.29	13.38	−19.65	25.47	1.89	11.93	−21.10
MCG-03-34-013	40.7	0.495	0.364	0.264	22.33	0.23	15.50	−17.55	21.05	0.22	14.19	−18.86	20.45	0.22	13.61	−19.44

Notes.
[a] Distance of NGC 5018 is from Tully (1988); distances of NGC 5022 and MCG-03-34-013 are from NED.
[b] Extinction correction in the u, g, and r bands are from Burstein & Heiles (1982).
[c] Derived by integrating the growth curves and corrected for interstellar extinction.

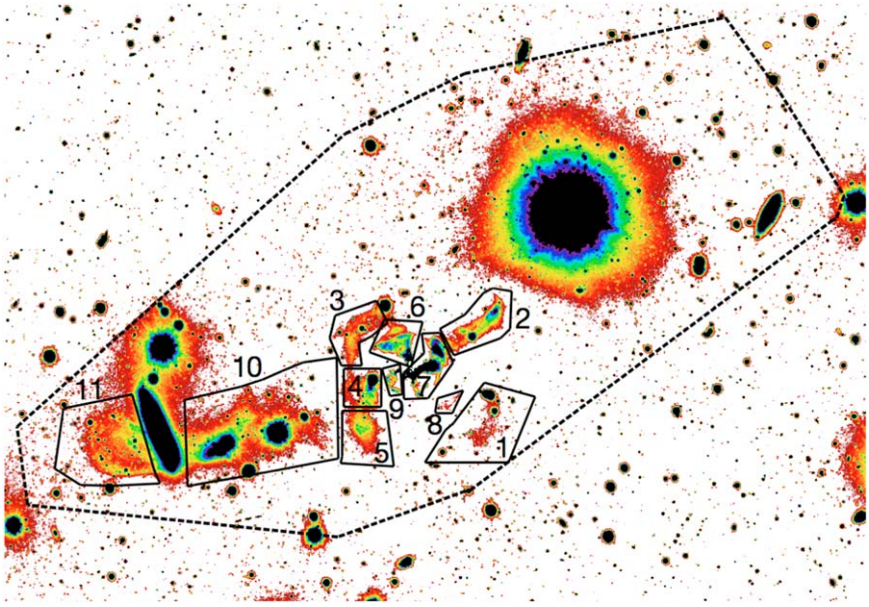

Figure 5. Residual image obtained by subtracting the galaxy model from the VST *g*-band image. The numbers indicate the most luminous substructures for which we have estimated the integrated colors (see Section 4.3). The dashed polygon marks the area over which we estimated the integrated magnitudes and colors of the intragroup component (see Section 4.4).

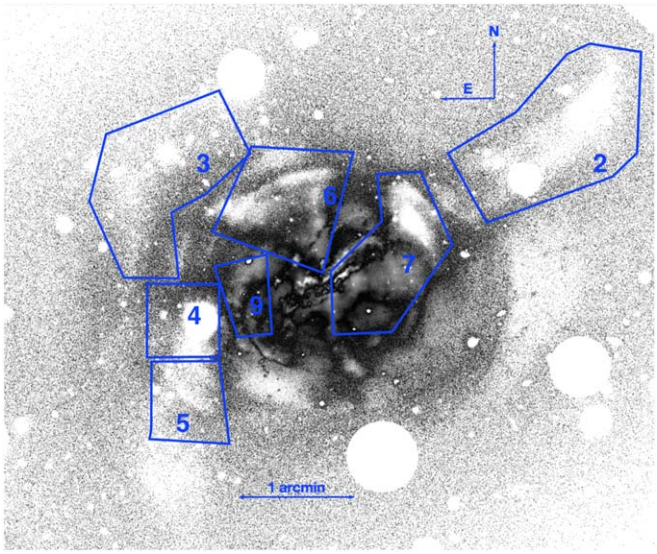

Figure 6. Result of the model-fitting and division method employed to quantify the tidal disturbance of NGC 5018 (see text). The image size is 6×5 arcmin^2. The overplotted blue contours mark the substructures shown in Figure 5, which are also visible in this image.

$((w1 - w2) = -0.06)$) and the loop (labelled as 11, $((w1 - w2) = 0.22)$), are not consistent with any of the galaxies in the group, as already found from the optical colors.

6. Ultraviolet Analysis for NGC 5022

In order to detect the presence of hot and young stars in the NGC 5018 group, we also performed a photometric analysis in the ultraviolet bands. The near-ultraviolet (NUV) profile of NGC 5018 has been published by Rampazzo et al. (2007), while the far-ultraviolet (FUV) profile is not published because of the low signal-to-noise ratio in the FUV band.

The FUV and NUV images of NGC 5022 used here were obtained from the *Galaxy Evolution Explorer* (*GALEX*) archive (see Martin et al. 2005; Morrissey et al. 2005). The exposure times were 4451 s in NUV and 1568 s in FUV bands (limiting magnitude in FUV/NUV $\sim$ 22.6/22.7 AB mag, Bianchi 2009).

We used FUV and NUV background-subtracted, intensity images derived from the *GALEX* pipeline. FUV and NUV magnitudes have been computed as $m(\mathrm{AB})_{\mathrm{UV}} = -2.5 \times \log \mathrm{CR}_{\mathrm{UV}} + \mathrm{ZP}$, where CR is the dead-time-corrected, flat-fielded count rate and the zero-points are ZP = 18.82 and ZP = 20.08 in the FUV and NUV respectively (Morrissey et al. 2007).

Both FUV and NUV surface photometry have been performed using the IRAF STSDAS ELLIPSE routine. The resulting surface brightness profiles are shown in Figure 11. Our measured NUV and FUV total magnitudes (NUV = 16.6 $\pm$ 0.03 and FUV = 17.4 $\pm$ 0.07) are consistent within errors with the one measured in *GALEX* General Release 6. Both luminosity profiles are well fitted by a disk with $n = 0.9$, where n is the Sérsic index (see the bottom panel of Figure 11).

As for the optical images, we use the IRAF task BMODEL to create a 2D image and then we subtract this model from the original one. The residual images are shown in Figure 12. As we can see in the final images (right panels), three bright regions are clearly visible in the southern part of the disk. We suspect these are regions of star formation. For this reason we measured the flux of the three blobs visible. As a comparison we measured the total NUV and FUV fluxes for the whole northern part of the galaxy.

Using the FUV flux, we derived the present-day star formation rate (SFR) of each UV-bright blob (see the bottom-right panel of Figure 12) following Kennicutt (1998), using its UV continuum luminosity and the relation $\mathrm{SFR}\ (M_{\odot}\,\mathrm{yr}^{-1}) = 1.4 \times 10^{-28}\, L_{\mathrm{FUV}}$ (erg s^{-1} Hz^{-1}). The final results are reported in Table 4. As we can see, the SFR is the same over the whole galaxy.

7. Total Accreted Mass in a Loose Group of Galaxies

Following the procedure adopted by Spavone et al. (2017), we have described the surface brightness profiles of NGC 5018

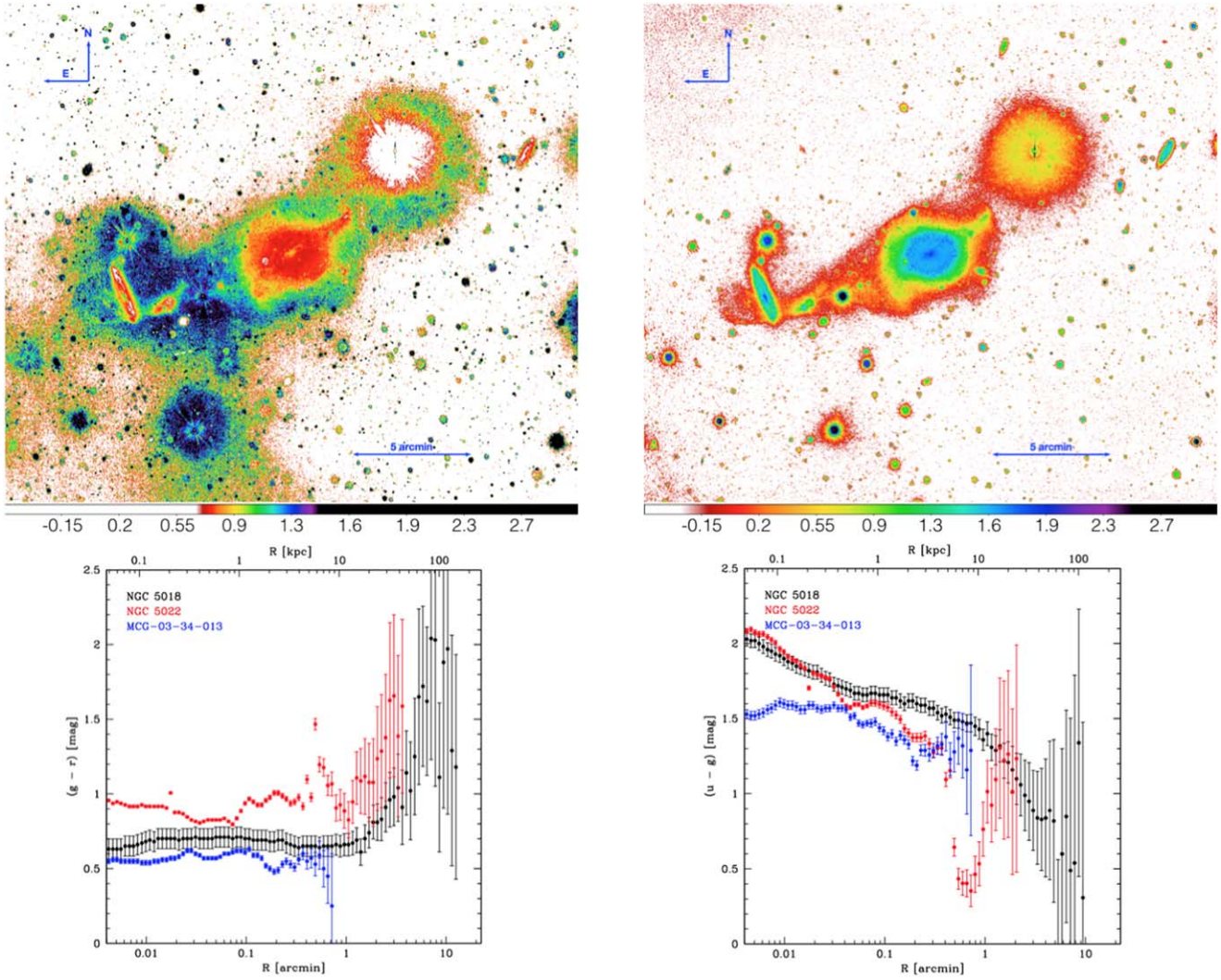

Figure 7. ($g - r$) (top-left panel) and ($u - g$) (top-right panel) color maps centered on NGC 5018. Bottom: azimuthally averaged, extinction-corrected, ($g - r$) (left) and ($u - g$) (right) color profiles of NGC 5018 (black), NGC 5022 (red), and MCG-03-34-013 (blue).

with a three-component model in order to define the different components dominating the galaxies' light distribution at different scales: a Sérsic profile (Sérsic 1963; Caon et al. 1993) for the centrally concentrated in situ stars, a second Sérsic for the "relaxed" accreted component, and another Sérsic component for the diffuse and "unrelaxed" outer envelope (Seigar et al. 2007; Donzelli et al. 2011; Arnaboldi et al. 2012; Cooper et al. 2015; Iodice et al. 2016; Spavone et al. 2017).

The stellar population of the central in situ component is expected to be similar to that of the dominant "relaxed" accreted component, while the outer diffuse component representing "unrelaxed" accreted material ("streams" and other coherent concentrations of debris) does not contribute significantly to the brighter regions of the galaxy.

For the central ETG, NGC 5018, we used the same fitting procedure described in Spavone et al. (2017), consisting in fixing $n \sim 2$ for the in situ component of our three-component fit, in order to mitigate the degeneracy in parameters in such a fit. This typical value of n has been adopted on the basis of the results of Cooper et al. (2013) for massive galaxies. The results of this fit for NGC 5018, with the corresponding (O – C) residuals, are shown in Figure 13, both on a logarithmic scale (top panel) and a linear one (bottom panel), while the best-fitting structural parameters for the fit are reported in Table 5. The result of the fit shows that the outer part of this galaxy's surface brightness profile is almost exponential in nature, and in fact we checked that fitting an outer exponential component to the surface brightness profile does not change the residuals or the shape of the total fitted profile.

The surface brightness profiles of NGC 5022 and MCG-03-34-013 have also been fitted with a three-component model and two-component model, respectively, in which all the parameters were left free. The results of the fit are shown in Figure 14 and the best-fitting parameters are reported in Table 5.

We used these fits to derive the total magnitude of the different Sérsic components, $m_{T,1}$, $m_{T,2}$, and $m_{T,3}$, as well as the relative contribution of the accreted component with respect to the total galaxy light, $f_{h,T}$, reported in Table 5. The total accreted mass fraction for the galaxies in this small group ranges between 78% and 92%. These values are consistent with the results of numerical simulations, which predict that stars accreted by BCGs account for most of the total stellar mass of the galaxy (Cooper et al. 2013, 2015; Pillepich et al. 2018).

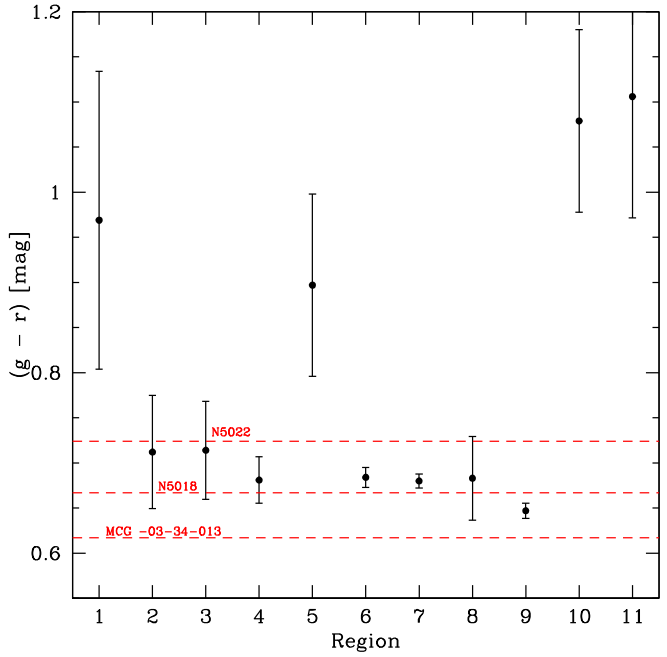

Figure 8. Integrated ($g - r$) colors in the 11 regions marked on the residual image, Figure 5. Red dashed lines represent the integrated colors of the three main galaxies in the VST field (see Figure 1): NGC 5018, NGC 5022, and MCG-03-34-013.

These results can be used to estimate the stellar mass fractions in the different components by assuming appropriate stellar mass-to-light ratios, in order to compare the accreted mass ratios we infer from our observations with other observational estimates for BCGs of similar total mass by Seigar et al. (2007), Bender et al. (2015), Iodice et al. (2016), and Spavone et al. (2017), and with theoretical predictions from semi-analytic particle-tagging simulations by Cooper et al. (2013, 2015), and the Illustris cosmological hydrodynamical simulations (Pillepich et al. 2018).

To this aim, we measured the mean ($u - g$) and ($g - r$) colors for each galaxy in regions where the central galaxies and the outer envelopes dominate, obtaining the values reported in Table 6. We then used stellar population synthesis models (Ricciardelli et al. 2012; Vazdekis et al. 2012), with a Kroupa initial mass function to derive the mass-to-light ratios corresponding to the average colors, and hence the stellar mass of the whole galaxy and of the outer envelope. These results are summarized in Table 6 and the comparison is shown in Figure 15. Simulations used to compare the stellar halo mass fraction of our galaxies cover scales from the stellar halos of Milky Way-like galaxies to the cD envelopes of groups and clusters. For this reason the comparison shown in Figure 15 is meaningful only for the most massive galaxy of the group.

We find that the stellar mass fraction of the accreted component derived for the three main galaxies in the NGC 5018 group is fully consistent both with published data for other BCGs (Seigar et al. 2007; Bender et al. 2015; Iodice et al. 2016; Spavone et al. 2017), despite considerable differences in the techniques and assumptions involved, and with the theoretical models by Cooper et al. (2013, 2015) and by Pillepich et al. (2018).

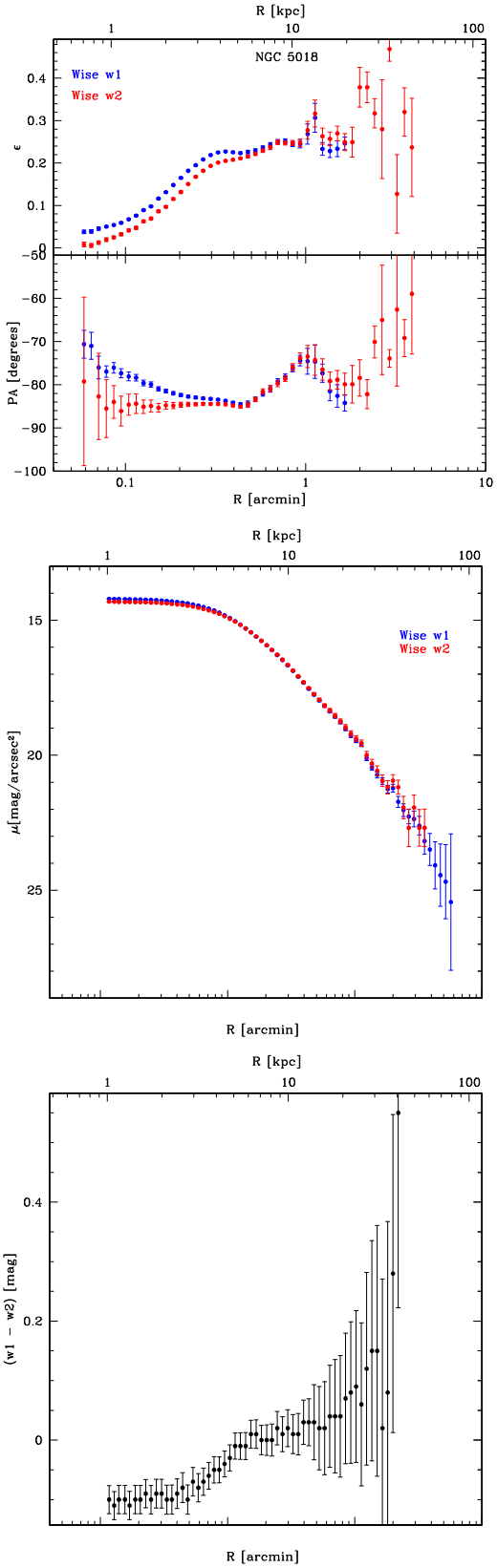

Figure 9. Top: ellipticity (ϵ) and position angle (P.A.) profiles for NGC 5018, in the *WISE w1* (3.368 μm, blue points) and *w2* (4.618 μm, red points) bands. Middle: azimuthally averaged surface brightness profiles in the *w1* and *w2* bands. Bottom: azimuthally averaged color profile.

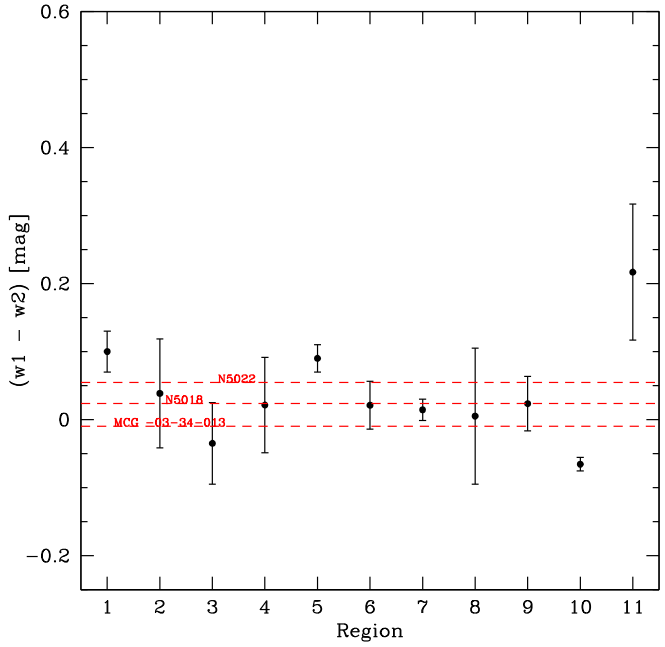

Figure 10. The same as Figure 8 for the *WISE w1* band.

8. Discussion and Conclusions

In this work we present a new deep mosaic of 1.2 × 1.0 square degrees of the group of galaxies centered on NGC 5018, acquired at the ESO VLT Survey Telescope. Taking advantage of the deep and multiband photometry (in *u, g, r* bands) and of the large field of view of the VST telescope, we study the structure of the galaxy members and the faint features leading into the intragroup space, and then we give an estimate of the intragroup diffuse light in the NGC 5018 group of galaxies.

8.1. Tracing the Growth History of the Group

NGC 5018, sometimes classified as E3, and NGC 5022 to the southeast, which is an edge-on spiral, seem to be linked by a filament of very low surface brightness. Indeed, many sources in the literature identify these two galaxies as an interacting pair.

The spiral to the southeast shows no warp or obvious signs of interaction, while N5018 exhibits a perturbed morphology in the outskirts, with shells and ripples, as well as inner dust signs. The H I map from the VLA (Figure 1) indicates that there is a long tail of gas that connects NGC 5022 to another group member, MCG-03-34-013, to the northwest of NGC 5018. Such an H I filament is to the north and does not cross NGC 5018, although a branch of it does enter the galaxy. Therefore, one open issue in the formation history of the group is whether the tails and all intragroup features visible in the light distribution trace the same interaction traced by the cold gas filaments.

Taking advantage of the multiband observations from VEGAS, we are able to estimate the integrated colors of all the intragroup features (see Section 4.4). We found that the integrated optical colors of all substructures (see Figure 5) are not consistent with the average colors of any of the galaxies in the group, being redder. This is confirmed by estimating the NIR integrated colors for the same regions and galaxies. Therefore, this finding suggests an external origin for them.

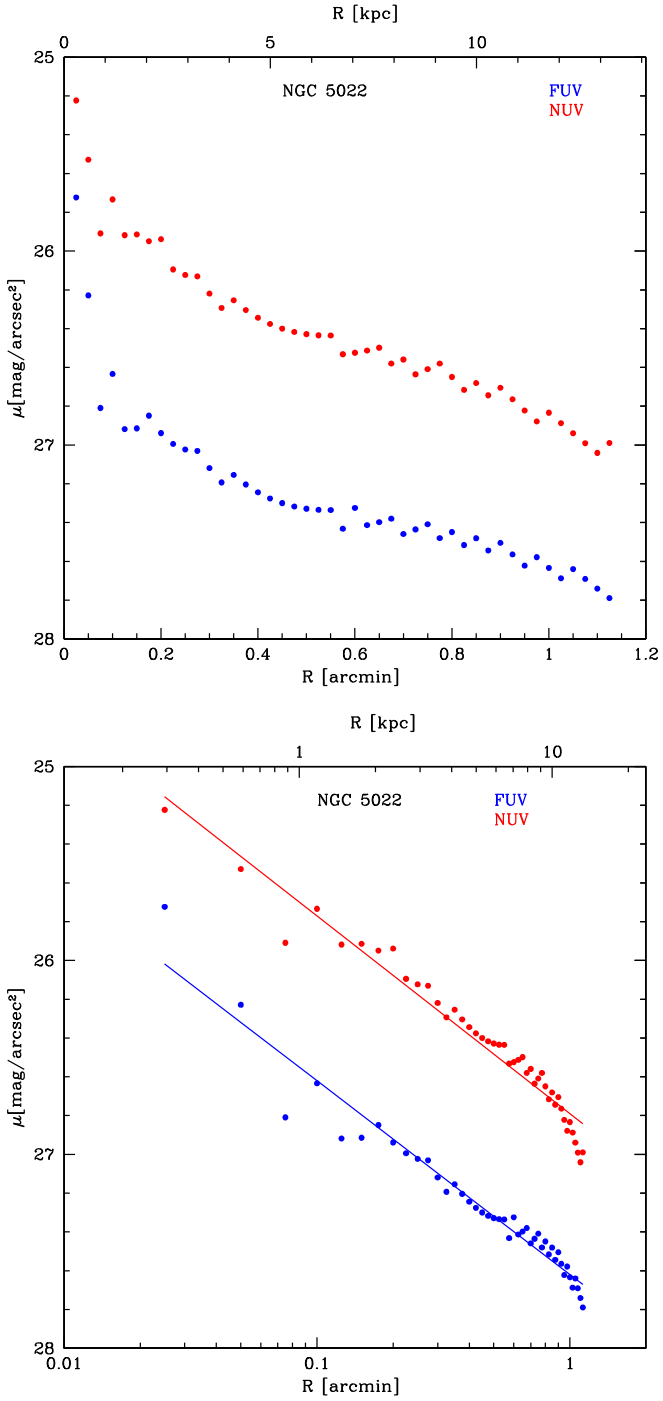

Figure 11. Top: azimuthally averaged surface brightness profiles in the FUV (blue points) and NUV (red points) bands. Bottom: the same profiles plotted on a logarithmic scale.

Something similar was found for the bright galaxy NGC 1316, in the SW subgroup of the Fornax cluster (Iodice et al. 2017b), where, by adopting the same approach based on the color analysis, the authors concluded that some of the substructures in the envelope come from the recent accretion of a smaller and bluer galaxy, while the large and redder tidal tail is more reasonably related to an earlier interaction event.

In NGC 5018, the analysis of the integrated colors suggests that the plume to the NW side and all the substructures in its central spheroid are coeval with the galaxy, given that they have comparable colors. These features can thus be interpreted

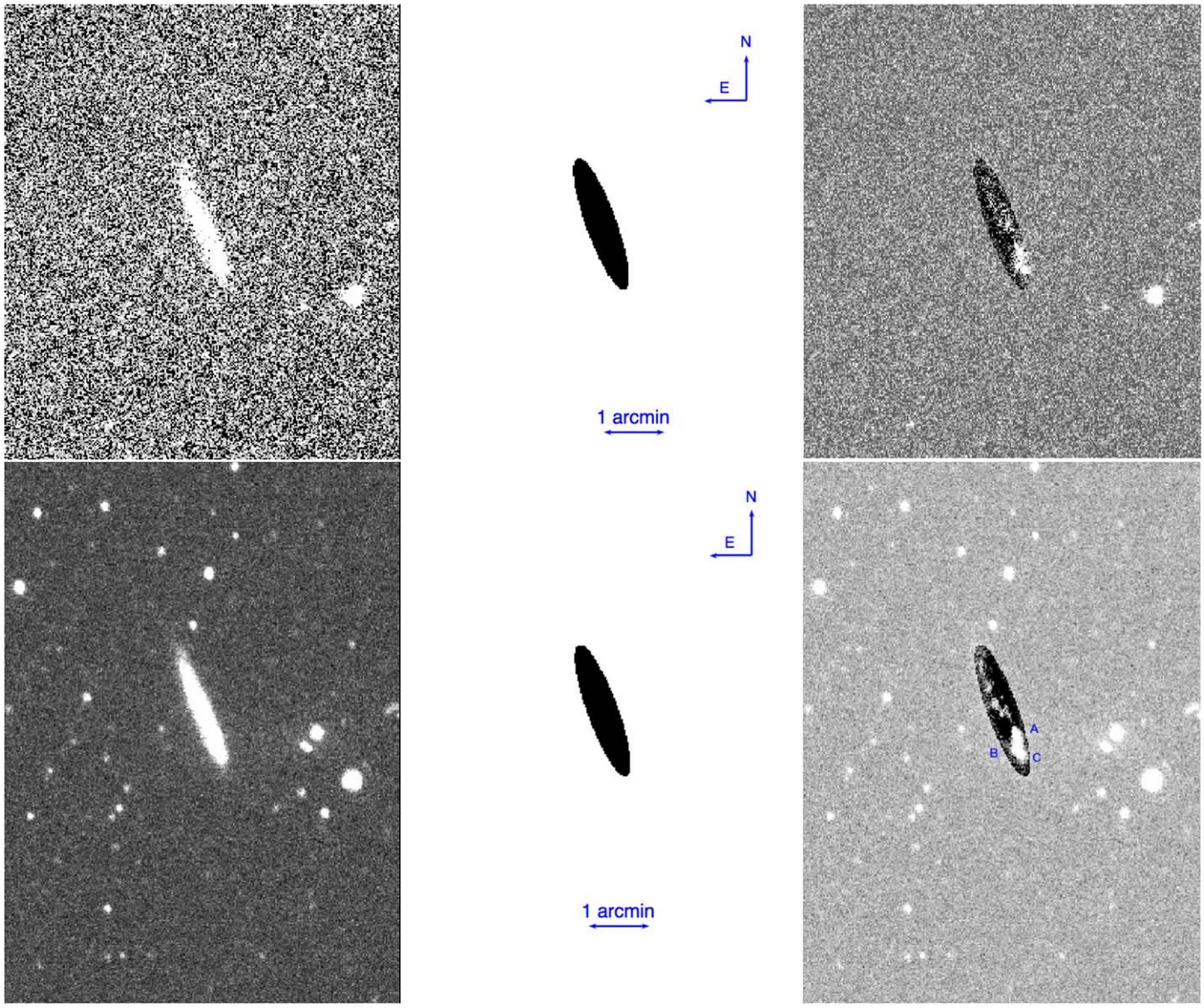

Figure 12. Top: FUV image of NGC 5022 (left), 2D model of the galaxy (middle), residual of the subtraction of the model (right). Bottom: NUV image of NGC 5022 (left), 2D model of the galaxy (middle), residual of the subtraction of the model (right).

as material expelled from NGC 5018 during a merging event in its formation history. In contrast, the bridge between NGC 5018 and NGC 5022, the diffuse loop on the east side of NGC 5022, and the patches numbered 1 and 5 to the east and SW sides (see Figure 5) have both optical and NIR colors not consistent with the average colors of any of the galaxies in the group, which are in the range $(g - r) \sim 0.6$–0.75 mag, being redder ($(g - r) \sim 0.9$–1.1 mag, see Figure 8). They are more similar to the colors in the outskirts of NGC 5018 and NGC 5022, which are $(g - r) \sim 0.9$–1.4 mag for $1 \leqslant R \leqslant 4$ arcmin (see Figure 7). Therefore, we claim that such a feature could be created by material stripped from the galaxy outskirts in a close passage. In particular, the almost polar half-ring on the east side of NGC 5022 could be formed by interaction with a highly inclined orbit (see, e.g., Bournaud & Combes 2003). Moreover, such an interaction might have triggered the regions of new star formation in the southern part of NGC 5022, as found from the analysis of the UV data (see Section 6).

On the other hand, the long tail of H I gas traces the interaction between NGC 5022 and MCG-03-34-013 (see also Kim et al. 1988; Guhathakurta et al. 1990).

8.2. Estimates of Total Accreted Mass and Intragroup Light

According to Spavone et al. (2017), by fitting the surface brightness profile of NGC 5018 with three Sérsic components, we were able to get an estimate of the total accreted mass in this galaxy, which is the brightest group member, and for all the less bright galaxies (see Section 7). We found that the total accreted mass fraction for the galaxies in this small group ranges between 78% and 92%. These values are consistent with the results of numerical simulations by Cooper et al. (2013, 2015) and Pillepich et al. (2018) and with published data for other BCGs (Seigar et al. 2007; Bender et al. 2015; Iodice et al. 2016; Spavone et al. 2017), despite considerable differences in the techniques and assumptions involved (see Figure 15).

Table 4
Integrated Photometric UV Properties

Object	R.A. (2000)	Decl. (2000)	m_{FUV}(AB)	F_{FUV}	L_{FUV}	m_{NUV}(AB)	F_{NUV}	L_{NUV}	FUV – NUV	SFR_{FUV}
Galaxy	198.38	−19.54	17.4 ± 0.07	1.84	4.08	16.6 ± 0.03	1.27	2.82	0.8	5.7
A	198.373	−19.5578	18.42 ± 0.19	0.75	1.64	17.64 ± 0.21	0.65	1.44	0.92	2.32
B	198.3748	−19.5563	17.86 ± 0.14	1.13	2.5	17.5 ± 0.11	0.74	1.64	0.59	3.5
C	198.3741	−19.5528	18.02 ± 0.09	0.98	2.18	17.27 ± 0.08	1.00	2.22	0.75	3.05

Note. (1) Coordinates are given in degrees. (2) Fluxes are in units of 10^{-27} erg s^{-1} cm^{-2} Hz^{-1}. (3) Luminosities are in units of 10^{26} erg s^{-1} Hz^{-1}. (4) SFRs are in units of $10^{-2}\,M_{\odot}$ yr^{-1}.

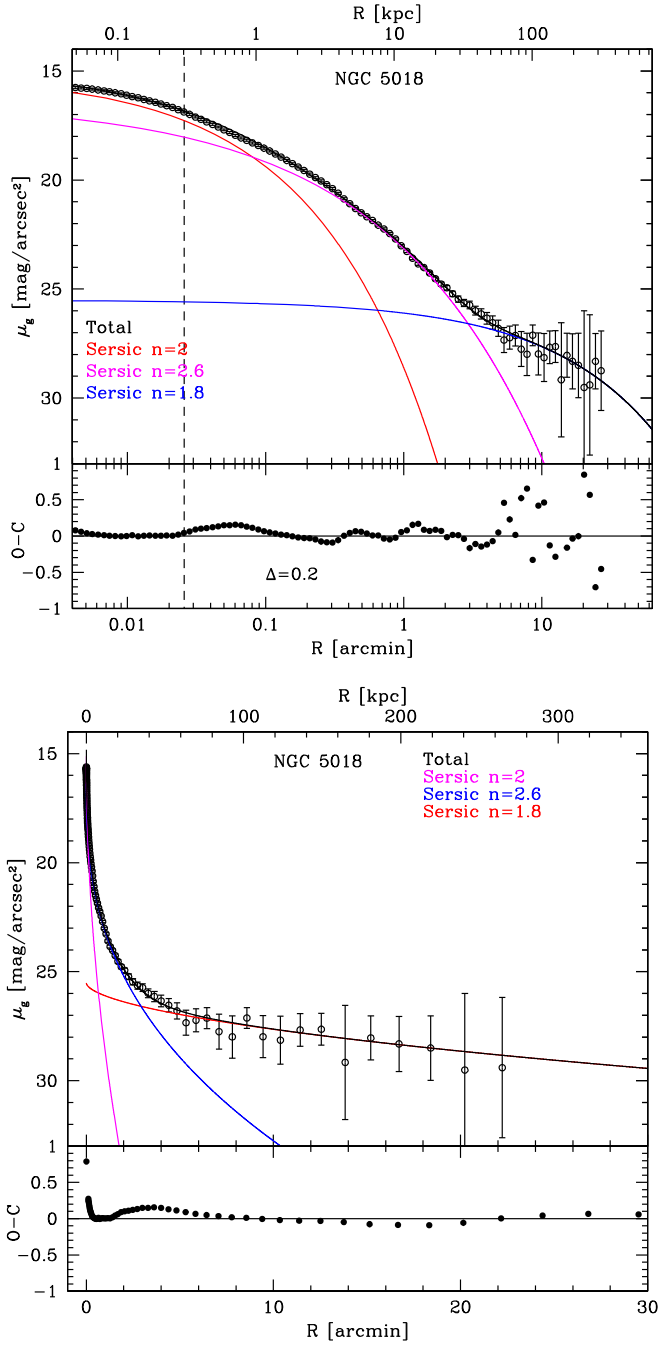

Figure 13. VST g-band profile of NGC 5018, on a logarithmic scale (top) and a linear one (bottom), fitted with a three-component model motivated by the predictions of theoretical simulations (see Spavone et al. 2017). The dashed line indicates the core of the galaxy, which was excluded in the fit.

The change in the trend of the ellipticity and P.A. with radius appears to correlate with an inflection in the surface brightness profile of NGC 5018, which also marks the transition between the two accreted components in the fit of the light distribution (see Figure 13). As already pointed out in Spavone et al. (2017), such an inflection could mark the transition between two components in different states of dynamical relaxation. The upward inflection of the profile over the transition radius occurs well beyond $2R_e$, suggesting an excess of weakly bound stars associated with a recent accretion event. NGC 5018 shows clear signs of ongoing interaction and accretion events, indicating that its outer regions are still being assembled, consistent with theoretical expectations for such galaxies (e.g., Cooper et al. 2015).

The total g-band luminosity of the IGL is $L_g^{\rm IGL} = 7.06 \times 10^{10}\,L_{\odot}$, which is ∼41% of the total luminosity of the group. The IGL has $(g-r) = 0.78 \pm 0.35$ mag, which is similar to the color in the halo of the BCG in the group core, NGC 5018, and consistent with the integrated colors of the other galaxies in the group. This is consistent with that found in many compact groups of galaxies (White et al. 2003; Da Rocha & Mendes de Oliveira 2005; Da Rocha et al. 2008), and with the prediction of numerical simulations (Sommer-Larsen 2006). The presence of IGL indicates that tidal encounters stripped a considerable amount of mass from the member galaxies, and that the group is in an advanced stage of its dynamical evolution (Da Rocha & Mendes de Oliveira 2005; Rudick et al. 2006; Sommer-Larsen 2006). Slow encounters in a group environment are in fact effective in liberating stars in the intragroup medium, and since the fraction of IGL increases with the degree of dynamical evolution of the group/cluster, it can be used as a "dynamical clock": more evolved groups/clusters have larger fractions of diffuse light.

Moreover, as already argued by Krick & Bernstein (2007), the color of IGL and its correlation with the color of galaxies in the group could help to constrain the epoch at which stars forming the IGL were stripped. In the case of NGC 5018, since the color of the IGL component is consistent with those of galaxies belonging to the group, the ongoing stripping scenario is the most plausible for the formation of IGL in this system.

As a concluding remark, the picture emerging from the multi-wavelength study illustrated in this work is that there are at least two different interactions involving the group members: one between the two brightest galaxies NGC 5018 and NGC 5022, which generates the tails and ring-like structures detected in the light, and another between the two gas-rich galaxies of the group, NGC 5022 and MCG-03-34-013, which has produced the long H I tail connecting the two systems. Moreover, a minor merging event also happened in the

Table 5
Best-fitting Structural Parameters for a Three-component Fit

Object	μ_{e1} (mag arcsec^{-2})	r_{e1} (arcsec)	n_1	μ_{e2} (mag arcsec^{-2})	r_{e2} (arcsec)	n_2	μ_{e3} (mag arcsec^{-2})	r_{e3} (arcsec)	n_3	$m_{T,1}$ (mag)	$m_{T,2}$ (mag)	$m_{T,3}$ (mag)	$f_{h,T}$
NGC 5018	19.10 ± 0.10	5.24 ± 0.07	2	21.67 ± 0.34	31.75 ± 0.50	2.6 ± 0.1	29.06 ± 0.20	1502 ± 7	1.8 ± 0.2	12.16	10.77	9.79	92%
NGC 5022	20.15 ± 0.50	3.00 ± 0.20	1.26 ± 0.35	21.55 ± 1.27	12.27 ± 2.90	0.60 ± 0.20	26.38 ± 0.32	87.61 ± 7.6	3.00 ± 0.62	14.38	12.72	13.28	88%
MCG-03-34-013	21.70 ± 0.06	12.09 ± 2.00	0.50 ± 0.34	22.18 ± 0.18	11.55 ± 0.02	1.25 ± 0.03	⋯	⋯	⋯	12.16	10.77	⋯	78%

Note. Columns 2–4 report effective magnitude and effective radius for the inner component of each fit. The Sérsic index for the in situ component of the BCG NGC 5018 was fixed to $n \sim 2$ using the models as a prior (Cooper et al. 2013), as explained in Spavone et al. (2017). We allowed small variations of ± 0.5 around the mean value of $n = 2$. This would bracket the range of n in the simulations and allows us to obtain a better fit. Columns 5–10 list the same parameters for the second and the third components. Columns 11–13 report the total magnitude of the inner ($m_{T,1}$) and outer Sérsic components ($m_{T,2}$ and $m_{T,3}$). Column 14 gives the total accreted mass fraction derived from our fit.

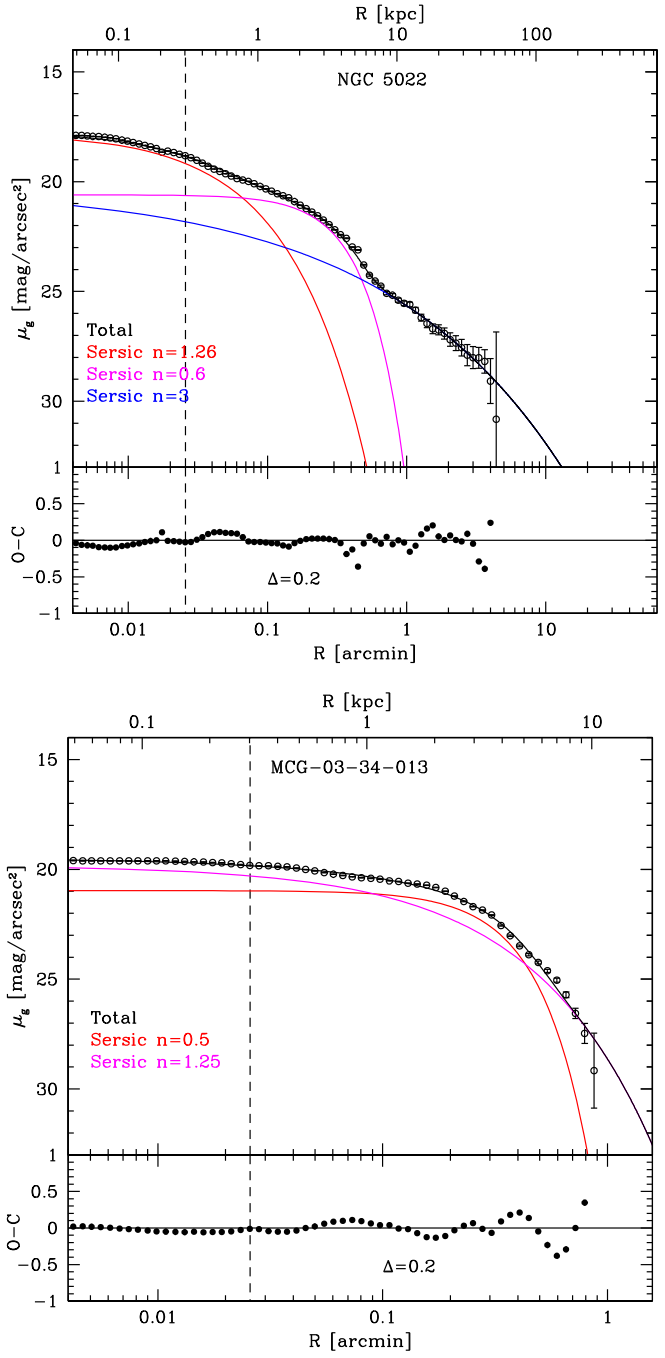

Figure 14. VST g-band profiles of NGC 5022 (top), fitted with a three-component model, and MCG-03-34-013 (bottom), fitted with a double Sérsic model.

formation history of NGC 5018 that has perturbed the inner structure of this galaxy.

The unperturbed isophotes of MCG-03-34-013 would suggest that the interaction involving such a small galaxy with NGC 5022 is more likely a high-velocity encounter between them, while the gravitational forces between the two bright group members were strong enough to perturb the outskirts and generate intragroup material.

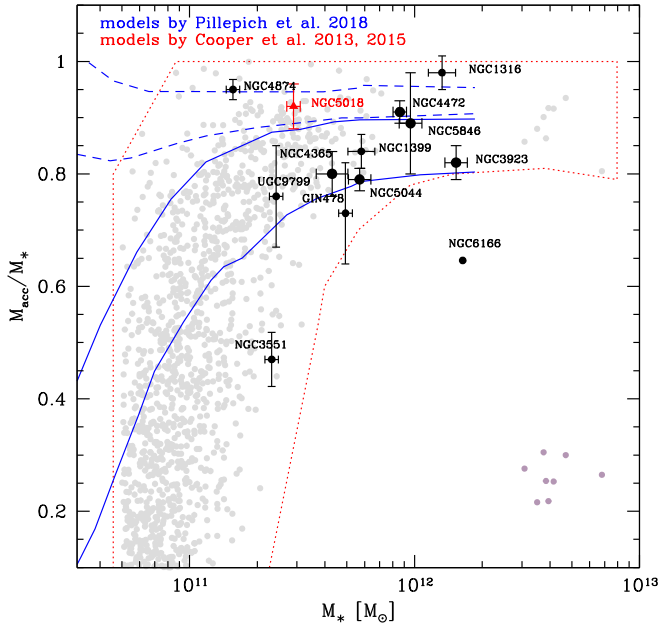

Figure 15. Accreted mass fraction vs. total stellar mass for ETGs. The measurement for NGC 5018 is given as a red triangle. Black circles correspond to other BCGs from the literature (Seigar et al. 2007; Bender et al. 2015; Iodice et al. 2016; Spavone et al. 2017). The red region indicates the predictions of simulations of cosmological galaxy formation by Cooper et al. (2013, 2015). Blue continuous and dashed regions indicate the accreted mass fraction measured within 30 kpc and outside 100 kpc, respectively, in Illustris simulations by Pillepich et al. (2018) (see their Figure 12). Purple-gray points show the mass fraction associated with the streams from Table 1 in Cooper et al. (2015).

Table 6
Total and Accreted Stellar Masses of Galaxies in Our Sample

Object	$(u-g)$ (mag)	$(g-r)$ (mag)	$(M/L)_g$ $(M_\odot/L_\odot)$	$M^*_{\rm tot}$ $(M_\odot)$	$M^*_{\rm total\ accreted}$ $(M_\odot)$
NGC 5018	1.6 ± 0.4	0.7 ± 0.2	1.97	2.9×10^{11}	2.7×10^{11}
NGC 5022	1.0 ± 0.4	1.6 ± 0.5	1.48	1.6×10^{10}	1.4×10^{10}
MCG-03-34-013	0.6 ± 0.1	1.4 ± 0.1	0.82	4.3×10^{9}	3.3×10^{9}

Note. Columns 2, 3, and 4 show the mean, extinction-corrected, $(u-g)$ and $(g-r)$ colors of each galaxy and the relative mass-to-light ratio in the g-band. Columns 5 is the stellar mass of the galaxy, while column 6 reports the total accreted stellar masses, derived from the three- and two-component fits.

We are very grateful to the anonymous referee for his/her comments and suggestions, which helped us to improve and clarify our work. This work is based on visitor mode observations taken at the ESO La Silla Paranal Observatory within the VST Guaranteed Time Observations, Programme IDs 096.B-0582(B), 097.B-0806(A), and 099.B-0560(A). M.S. wishes to thank the ESO staff of the Paranal Observatory for their support during the observations at VST. M.S. acknowledges financial support from the VST project (P.I. P. Schipani). R.R. and D.B. acknowledge funding from the INAF PRIN-SKA 2017 program 1.05.01.88.04. This publication makes use of data products from the *Wide-field Infrared Survey Explorer*, which is a joint project of the University of California, Los

Angeles, and the Jet Propulsion Laboratory/California Institute of Technology, funded by the National Aeronautics and Space Administration.

ORCID iDs

Marilena Spavone https://orcid.org/0000-0002-6427-7039
Enrichetta Iodice https://orcid.org/0000-0003-4291-0005
Daniela Bettoni https://orcid.org/0000-0002-4158-6496
Michele Cantiello https://orcid.org/0000-0003-2072-384X
Luca Limatola https://orcid.org/0000-0002-1896-8605
Aniello Grado https://orcid.org/0000-0002-0501-8256
Pietro Schipani https://orcid.org/0000-0003-0197-589X

References

Aguerri, J. A. L., Castro-Rodríguez, N., Napolitano, N., Arnaboldi, M., & Gerhard, O. 2006, A&A, 457, 771
Aguerri, J. A. L., Gerhard, O. E., Arnaboldi, M., et al. 2005, AJ, 129, 2585
Arnaboldi, M., Aguerri, J. A. L., Napolitano, N. R., et al. 2002, AJ, 123, 760
Arnaboldi, M., Gerhard, O., Aguerri, J. A. L., et al. 2004, ApJL, 614, L33
Arnaboldi, M., Ventimiglia, G., Iodice, E., Gerhard, O., & Coccato, L. 2012, A&A, 545, AA37
Bender, R., Kormendy, J., Cornell, M. E., & Fisher, D. B. 2015, ApJ, 807, 56
Bertola, F., Burstein, D., & Buson, L. M. 1993, ApJ, 403, 573
Bianchi, L. 2009, Ap&SS, 320, 11
Bournaud, F., & Combes, F. 2003, A&A, 401, 817
Burstein, D., & Heiles, C. 1982, AJ, 87, 1165
Buson, L. M., Bertola, F., Bressan, A., Burstein, D., & Cappellari, M. 2004, A&A, 423, 965
Cantiello, M., D'Abrusco, R., Spavone, M., et al. 2018, A&A, 611, A93
Caon, N., Capaccioli, M., & D'Onofrio, M. 1993, MNRAS, 265, 1013
Capaccioli, M., Spavone, M., Grado, A., et al. 2015, A&A, 581, A10
Carollo, C. M., & Danziger, I. J. 1994, MNRAS, 270, 743
Castro-Rodríguez, N., Aguerri, J. A. L., Arnaboldi, M., et al. 2003, A&A, 405, 803
Castro-Rodriguéz, N., Arnaboldi, M., Aguerri, J. A. L., et al. 2009, A&A, 507, 621
Contini, E., De Lucia, G., Villalobos, Á., & Borgani, S. 2014, MNRAS, 437, 3787
Cooper, A. P., D'Souza, R., Kauffmann, G., et al. 2013, MNRAS, 434, 3348
Cooper, A. P., Gao, L., Guo, Q., et al. 2015, MNRAS, 451, 2703
Da Rocha, C., & Mendes de Oliveira, C. 2005, MNRAS, 364, 1069
Da Rocha, C., Ziegler, B. L., & Mendes de Oliveira, C. 2008, MNRAS, 388, 1433
D'Abrusco, R., Cantiello, M., Paolillo, M., et al. 2016, ApJL, 819, L31
De Lucia, G., Springel, V., White, S. D. M., Croton, D., & Kauffmann, G. 2006, MNRAS, 366, 499
DeMaio, T., Gonzalez, A. H., Zabludoff, A., et al. 2018, MNRAS, 474, 3009
Donzelli, C. J., Muriel, H., & Madrid, J. P. 2011, ApJS, 195, 15
Duc, P.-A., Cuillandre, J.-C., Karabal, E., et al. 2015, MNRAS, 446, 120
Feldmeier, J. J., Mihos, J. C., Morrison, H. L., Rodney, S. A., & Harding, P. 2002, ApJ, 575, 779
Ferrarese, L., Côté, P., Cuillandre, J.-C., et al. 2012, ApJS, 200, 4
Gerhard, O., Arnaboldi, M., Freeman, K. C., et al. 2005, ApJL, 621, L93
Gerhard, O., Arnaboldi, M., Freeman, K. C., et al. 2007, A&A, 468, 815
Ghosh, K. K., Swartz, D. A., Tennant, A. F., Wu, K., & Saripalli, L. 2005, ApJ, 623, 815
Gourgoulhon, E., Chamaraux, P., & Fouque, P. 1992, A&A, 255, 69
Grado, A., Capaccioli, M., Limatola, L., & Getman, F. 2012, MSAIS, 19, 362
Guhathakurta, P., Knapp, G. R., van Gorkom, J. H., & Kim, D.-W. 1990, in NASA Conf. Pub. 3084, The Interstellar Medium in External Galaxies: Summaries of Contributed Papers, Proc. Second Wyoming Conf., July 3–7, 1989, ed. D. J. Hollenbach & H. A. Thronson Jr. (Mountain View, CA: Ames Research Center), 26
Hilker, M., & Kissler-Patig, M. 1996, A&A, 314, 357
Ibata, R. A., Lewis, G. F., McConnachie, A. W., et al. 2014, ApJ, 780, 128
Iodice, E., Capaccioli, M., Grado, A., et al. 2016, ApJ, 820, 42
Iodice, E., Spavone, M., Cantiello, M., et al. 2017a, ApJ, 851, 75
Iodice, E., Spavone, M., Capaccioli, M., et al. 2017b, ApJ, 839, 21
Kennicutt, R. C., Jr. 1998, ARA&A, 36, 189
Kim, D.-W., Jura, M., Guhathakurta, P., Knapp, G. R., & van Gorkom, J. H. 1988, ApJ, 330, 684
Krick, J. E., & Bernstein, R. A. 2007, AJ, 134, 466
Krick, J. E., Bernstein, R. A., & Pimbblet, K. A. 2006, AJ, 131, 168
La Barbera, F., Ferreras, I., de Carvalho, R. R., et al. 2012, MNRAS, 426, 2300
Leonardi, A. J., & Worthey, G. 2000, ApJ, 534, 650
Lin, Y.-T., & Mohr, J. J. 2004, ApJ, 617, 879
Longobardi, A., Arnaboldi, M., Gerhard, O., et al. 2013, A&A, 558, A42
Longobardi, A., Arnaboldi, M., Gerhard, O., & Hanuschik, R. 2015, A&A, 579, A135
Malin, D. F., & Carter, D. 1983, ApJ, 274, 534
Martin, D. C., Fanson, J., Schiminovich, D., et al. 2005, ApJL, 619, L1
McGee, S. L., & Balogh, M. L. 2010, MNRAS, 403, L79
Merritt, A., van Dokkum, P., Danieli, S., et al. 2016, ApJ, 833, 168
Mihos, C. 2015, IAUGA, 22, 2247903
Mihos, J. C., Harding, P., Feldmeier, J., & Morrison, H. 2005, ApJL, 631, L41
Morrissey, P., Conrow, T., Barlow, T. A., et al. 2007, ApJS, 173, 682
Morrissey, P., Schiminovich, D., Barlow, T. A., et al. 2005, ApJL, 619, L7
Muñoz, R. P., Eigenthaler, P., Puzia, T. H., et al. 2015, ApJL, 813, L15
Murante, G., Arnaboldi, M., Gerhard, O., et al. 2004, ApJL, 607, L83
Murante, G., Giovalli, M., Gerhard, O., et al. 2007, MNRAS, 377, 2
Napolitano, N. R., Pannella, M., Arnaboldi, M., et al. 2003, ApJ, 594, 172
Okamoto, S., Arimoto, N., Ferguson, A. M. N., et al. 2015, ApJL, 809, L1
Pillepich, A., Nelson, D., Hernquist, L., et al. 2018, MNRAS, 475, 648
Pohlen, M., & Trujillo, I. 2006, A&A, 454, 759
Purcell, C. W., Bullock, J. S., & Zentner, A. R. 2007, ApJ, 666, 20
Rampazzo, R., Marino, A., Tantalo, R., et al. 2007, MNRAS, 381, 245
Rampazzo, R., Panuzzo, P., Vega, O., et al. 2013, MNRAS, 432, 374
Ricciardelli, E., Vazdekis, A., Cenarro, A. J., & Falcón-Barroso, J. 2012, MNRAS, 424, 172
Rudick, C. S., Mihos, J. C., & McBride, C. 2006, ApJ, 648, 936
Seigar, M. S., Graham, A. W., & Jerjen, H. 2007, MNRAS, 378, 1575
Sérsic, J. L. 1963, BAAA, 6, 41
Smith, B. J., Campbell, K., Struck, C., et al. 2018, AJ, 155, 81
Sommer-Larsen, J. 2006, MNRAS, 369, 958
Spavone, M., Capaccioli, M., Napolitano, N. R., et al. 2017, A&A, 603, A38
Tal, T., van Dokkum, P. G., Nelan, J., & Bezanson, R. 2009, AJ, 138, 1417
Tollet, É., Cattaneo, A., Mamon, G. A., Moutard, T., & van den Bosch, F. C. 2017, MNRAS, 471, 4170
Tully, R. B. 1988, Nearby Galaxies Catalog (Cambridge: Cambridge Univ. Press)
Vazdekis, A., Ricciardelli, E., Cenarro, A. J., et al. 2012, MNRAS, 424, 157
Watkins, A. E., Mihos, J. C., & Harding, P. 2015, ApJL, 800, L3
Watkins, A. E., Mihos, J. C., Harding, P., & Feldmeier, J. J. 2017, ApJ, 836, 145
Watson, D. F., Berlind, A. A., & Zentner, A. R. 2012, ApJ, 754, 90
White, P. M., Bothun, G., Guerrero, M. A., West, M. J., & Barkhouse, W. A. 2003, ApJ, 585, 739
Williams, B. F., Ciardullo, R., Durrell, P. R., et al. 2007, ApJ, 656, 756
Willman, B., Governato, F., Wadsley, J., & Quinn, T. 2004, MNRAS, 355, 159
Wright, E. L., Eisenhardt, P. R. M., Mainzer, A. K., et al. 2010, AJ, 140, 1868
Zibetti, S., White, S. D. M., Schneider, D. P., & Brinkmann, J. 2005, MNRAS, 358, 949